Near-field characterization of photonic crystal waveguides

Sergey I. Bozhevolnyi[1] and Laurens Kuipers[2]

[1]Department of Physics and Nanotechnology, Aalborg University, Pontoppidanstræde 103, DK-9220 Aalborg East, Denmark

[2]Center for Nanophotonics, FOM Institute for Atomic and Molecular Physics (AMOLF), Kruislaan 407, 1098 SJ Amsterdam, Netherlands

Abstract

In the last few years, development of photonic crystal waveguides and structures has immensely progressed revealing many interesting optical phenomena and demonstrating numerous potential applications. We show how a scanning near-field optical microscope (SNOM) in collection mode can be used to investigate these powerful new optical structures, in particular photonic crystal waveguides (PhCWs). Unlike conventional far-field techniques, a SNOM can detect truly guided light propagating inside the structure without relying on scattering, and the SNOM imaging is thereby not restricted by the diffraction limit of half of the wavelength used. In contrast to regular input-output measurements the SNOM collects local optical information which is therefore not integrated or averaged because the light had propagated through the entire photonic structure, including possible in- and out-coupling waveguides. We show how intensity detection can be used to map mode profiles determine losses locally, gain insight into the Bloch nature of the propagating light and investigate more complex photonic crystal-based structures. Phase-sensitive detection allows the Bloch nature to be investigated in more detail as all the Bloch harmonics belonging to a single Bloch mode can be unravelled. Time-resolved SNOM measurements (pulse tracking measurements) allow pulse propagation to be visualized and phase- and group velocity to be

determined independently with the need for modelling. For certain optical frequencies ultraslow light can be observed. The possibilities and limitations of SNOM imaging for the characterization of PhCWs are discussed.

PACS: 42.70.Qs; 07.79.Fc

Keywords: Photonic band gap materials; Scanning near-field optical microscopy

**Corresponding author:*

Dr. S. I. Bozhevolnyi,

Department of Physics and Nanotechnology, Aalborg University

Pontoppidanstræde 103, DK-9220 Aalborg Øst, DENMARK

Fax: (+45) 98156502; Tel: (+45) 96359222; E-mail: sergey@physics.auc.dk

1. Introduction

Photonic crystals (PhCs) are artificial structures exhibiting periodic variation of the refractive index on the wavelength scale that can lead, within a certain wavelength range (called photonic band gap), to light reflection from and inhibition of light propagation inside these structures due to interference in multiple light scattering [1, 2]. From the point of view of solid state physics, the periodicity in a dielectric constant results in the photonic band gap (PBG) just like the periodicity in an electrostatic potential gives rise to the forbidden electronic energy band. Using the language of physical optics, the PBG effect in two and three dimensions can be viewed as an extension of Bragg reflection in one direction (e.g., occurring in lasers with distributed feedback), where it leads to a so-called stop gap, to Bragg diffraction of waves propagating in any direction. The PBG effect opens a way to control the flow of light on a wavelength scale by introducing various, e.g., line and point, defects in PhCs, forming thereby waveguides and cavities. Two-dimensional (2D) PhCs combined with the structures exhibiting light confinement in the third dimension, e.g., planar slab waveguides, have been intensively investigated during the last years with the purpose of realization of highly integrated photonic circuits [3-5]. Various conFigurations of PhC waveguides (PhCWs) formed by line defects in 2D PCs have been experimentally studied, and many important issues have been clarified [5]. In this context, accurate and reliable characterization of PhCWs and the corresponding optical phenomena becomes of prime importance. It should be noted though that most of the characterization methods used until recently were of *indirect* nature. This has limited the amount of accessible information and might even have compromised the validity of the conclusions reached.

Visualization of light propagation by imaging of the PhCW surface with a camera [6] was one of the first characterization techniques used to investigate light propagation along PhCWs. This method relies on the presence of (accidental) surface defects that can scatter the radiation

guided along a PhCW out of the surface plane towards the camera or is limited to imaging leaky modes above the so-called light line, resulting in a visible track along the PhCW whose average visibility is (roughly) proportional to the PhCW mode power. Light scattering out of the surface plane has been also facilitated with engineered defects, e.g., with a trench etched close to the output of PhCW structures [7]. This technique seems to be more reliable than the first one since the scattering efficiency is better controlled. Yet another approach to visualization of light propagation was based on intentional coupling to leaky modes which radiated from the PhCW top surface [8]. Imaging of the PhCW output edge with a camera [8] or a tapered fibre [9] was mainly employed to confirm that the light does go through a bent PhCW in question. The above techniques have been of great help during early PhCW investigations but are qualitative by their nature and, thus, only of limited use. However, for high-quality PhCW structures, one can significantly improve the first method by detecting the light scattered by *air holes* of the PhCW structure, an approach that was recently shown to provide accurate loss characterization [10].

Quantitative input-output measurements of the power of light being transmitted by a sample containing a PhCW structure are not without problems either, because the power level is determined not only by the PhCW transmission but also (and often mainly) by coupling light in and out of the sample and in and out of the PhCW structures. Relative measurements of the transmission spectra with and without a PhCW [11, 12] (or with and without a bend [13]) with subsequent normalization were considered to be generally reliable for loss measurements by calibrating away the aforementioned extrinsic effects. However the transmission efficiency found in this way may exceed 100% [11-13], indicating that accurate characterization of low-loss PhCWs with this technique is somewhat problematic. Alternatively, one can make use of the Fabry-Perot resonance technique that was successfully applied for quantitative measurements of the propagation loss in straight PhCWs [14] and the modal reflection in bent PhCWs [15]. The Fabry-Perot interference

method was also used to characterize the loss contributions of several consecutive waveguide elements [16] as well as to reveal extraordinary large group-velocity dispersion [17]. The latter was recently observed in time-domain experiments utilizing picosecond light pulses and autocorrelation detection [18]. As far as PhCW modal characteristics are concerned, conventional (far-field) imaging of the PhCW surface has been found suitable for mapping the dispersion diagram of the *leaky* (and, thereby, lossy) PhCW modes revealing Bloch wave components in the excited PhCW modes [19]. On the other hand, it is clear that a bound PhCW mode that, for a give optical frequency, has a propagation constant larger than that in air, i.e., it is below the light line, *cannot* be observed with far-field imaging techniques, because its field in air is *evanescent*. Its amplitude decays exponentially over a distance of the order of light wavelength. One way of accessing bound PhCW modes is to employ the evanescent field coupling between a tapered optical fibre and a PhCW [20].

Mapping of evanescent fields is one of the main applications of collection scanning near-field microscopy (SNOM), whose fibre probe is used to pick up a tiny fraction of optical (e.g., evanescent) field near the sample surface and detect it as a function of scanning coordinates. Since the first demonstration of SNOM imaging of evanescent fields of waveguide modes [21], the SNOM has been used in a number of studies concerned with waveguide modes in integrated optical components [22], including waveguide characterization at telecommunication wavelengths [23]. Moreover, using heterodyne detection phase-sensitive SNOM [23a] in combination with the use of ultrafast pulses, the propagation of femtosecond laser pulses inside waveguides has been visualized and tracked (both in time and in space) allowing for direct measurements of the group and phase velocities [24]. Along with the progress in SNOM instrumentation, the understanding of image formation in the collection SNOM has been significantly improved. A naïve point of view that SNOM images represent maps of the electric (near-) field intensity has evolved into a more

complicated picture based on the properly described image formation in the collection SNOM [25-27].

The use of SNOM techniques for investigations of complicated scattering phenomena occurring in PBG structures has first started with studies of optical transmission through 2D PhCs and the corresponding intensity distributions [28-30]. The SNOM imaging has also been applied to near-field probing of various PhC resonant structures [31-33] and the phenomenon of highly directional emission from subwavelength PhCWs [34]. As far as radiation guiding along PhCWs (which is a by far more complicated phenomenon than guiding along conventional photonic waveguides) is concerned, the potential of SNOM imaging to characterize PhCW modes has only recently been explored, first, with time-independent intensity measurements [35-38] and, lately, with phase-sensitive and time-resolved visualization of pulse propagation [39, 40, 40a, 40b].

In this review, we consider main principles of SNOM characterization of PhCW structures and present the most significant experimental results obtained recently. The paper is organized as follows. In section 2, a theoretical description of image formation in the collection SNOM is outlined for both intensity and phase-sensitive detection, and its implications to the interpretation of SNOM images are considered. In the following sections 3 and 4, the two main SNOM techniques used for PhCW characterization are described along with the most essential results of corresponding investigations, including local probing of Bloch harmonics, mode dispersion and loss characterization and real-space pulse tracking. The paper is terminated with our conclusions offered in section 5.

2. Image formation in the collection mode SNOM

Signal detection in the collection SNOM conFiguration is based, for both intensity and phase-sensitive detection, on scattering of an optical near field with a (coated or uncoated) fibre tip into a combination of guided fibre modes propagating toward a detection conFiguration. The latter represents either simply an intensity detector, in the case of intensity detection, or a combination of a (fibre) coupler, in which the signal field is mixed with a coherent reference field, and a detector, whose output allows one to determine the signal amplitude and phase (Fig. 1). For simplicity, let us limit ourselves to the case of the fibre tip being scanned at a fixed plane P that is parallel to the sample surface. It is convenient [25-27] to make a plane-wave decomposition of the probed field $\boldsymbol{E}$ at the scanning plane $z = z_t$ (z_t is the z-coordinate of the tip end):

$$\boldsymbol{E}(\boldsymbol{r}_p, z_t) = \frac{1}{4\pi^2} \iint \boldsymbol{F}(\boldsymbol{k}_p) \exp(i\boldsymbol{k}_p \cdot \boldsymbol{r}_p)\, d\boldsymbol{k}_p \quad , \tag{1}$$

where $\boldsymbol{r}_p = (x,y)$, $\boldsymbol{k}_p = (k_x,k_y)$ is the projection of the wave vector on the surface plane, and $\boldsymbol{F}(\boldsymbol{k}_p)$ is the vector amplitude of the appropriate plane-wave component of the incident field. Fibres are generally only weakly guiding (i.e., the index difference between the fibre core and its cladding is very small) so that the guided waves are approximately transverse electromagnetic (TEM) and the linearly polarized modes can be introduced. Considering a single-mode weakly guiding fibre that supports two (degenerate) modes with orthogonal polarizations, one can represent the field propagating in the fibre in the form of two modes that are linearly polarized along the x'- and y'-axes (Fig. 1):

$$\boldsymbol{A}(\boldsymbol{r}_p^t) = \frac{1}{4\pi^2} \iint \boldsymbol{H}(\boldsymbol{k}_p) \cdot \boldsymbol{F}(\boldsymbol{k}_p) \exp(i\boldsymbol{k}_p \cdot \boldsymbol{r}_p^t)\, d\boldsymbol{k}_p \quad , \tag{2}$$

where $\boldsymbol{A} = (A_{x'}, A_{y'})$ is the vector containing the amplitudes of the modes, $\boldsymbol{r}_p{}^t = (x_t, y_t)$ with x_t and y_t being the scanning coordinates of the probe tip, and $\boldsymbol{H}$ ($\boldsymbol{k}_p$) represents the amplitude-coupling

matrix that accounts for the contribution of each plane-wave component (with the wave-vector projection $\boldsymbol{k}_p$) to the mode amplitudes. In writing Eq. (2) we have made use of the approximation of a passive probe that does not perturb the optical fields to be imaged, found adequate in most cases of collection SNOM [25], in the sense that the presence of the probe does not significantly alter the distribution of the near field.

In the case of (conventional) intensity detection, the SNOM detected signal is proportional to the total light power carried by the two orthogonal fibre modes: $S(\boldsymbol{r}_p{}^t) \sim |\boldsymbol{A}(\boldsymbol{r}_p{}^t)|^2$. It is thus clear that, even in the passive probe approximation (i.e., in the absence of probe-sample coupling), the SNOM images, in general, do not represent the (electric) field intensity distributions existing near the sample surface. Only if the spatial Fourier spectrum of the collected optical field is sufficiently narrow and consisting of only one polarization (so that the amplitude-coupling matrix in Eq. (2) reduces to a constant factor), can one directly relate the SNOM image to the near-field intensity distribution [26]. Such a situation does, in fact, take place in a number of important practical applications, including mapping of surface electromagnetic waves [41] and waveguide modes, accounting for the apparent success of SNOM characterization of photonic components [21-24, 28-40]. It should be borne in mind though that, even in a seemingly straightforward case of two counter-propagating evanescent waves, a great care should be exercised in order to correctly interpret the obtained SNOM images [42].

In the case of phase-sensitive detection [24], one should take into account that the propagation of light in the fibre may result in further polarization conversion and that virtually any polarization state can be obtained at the fibre output by its bending and twisting. The output fibre field can thus be expressed as follows: $\boldsymbol{E}_{out} = \boldsymbol{T} \cdot \boldsymbol{A}$, where the propagation matrix $\boldsymbol{T}$ accounts for the additional polarization conversion in the fibre. This field is then projected on and mixed with a coherent reference field $\boldsymbol{E}_{ref}$ (often frequency shifted, e.g., in an acousto-optic cell, to allow

heterodyne detection) usually by means of a fibre coupler, whose output provides an access to the amplitude and the phase of $\boldsymbol{E}_{out}$ that is, of course, if $\boldsymbol{E}_{out} \cdot (\boldsymbol{E}_{ref})^* \neq 0$. This is important to realize, because for proper phase-sensitive measurements, the phase difference between the output fibre field and the phase of the probed near field should be constant. Therefore care needs to be taken that the phase is not disturbed while scanning and (!) that the scanning itself does not lead to a perturbation of the fibre modes and their relative amplitudes and phases. In general, the (two-component) *output* fibre field $\boldsymbol{E}_{out}(\boldsymbol{r}_p^t)$ is *conceptually different* from the (three-component) *probed* field $\boldsymbol{E}(\boldsymbol{r}_p)$ with respect to polarization, phase and magnitude, so that one should be careful in the interpretation of the experimental results obtained [26, 27].

Let us consider the simplest case of detection of a single (propagating or evanescent) plane wave at $z = z_t$: $\boldsymbol{E}(\boldsymbol{r}_p,z_t) = \boldsymbol{E}_0 \exp(i\boldsymbol{\beta} \cdot \boldsymbol{r}_p)$. The output fibre field can then be represented as follows [Eqs. (1) and (2)]: $\boldsymbol{E}_{out}(\boldsymbol{r}_p^t) = \boldsymbol{T} \cdot (\boldsymbol{H}(\boldsymbol{\beta}) \cdot \boldsymbol{E}_0) \exp(i\boldsymbol{\beta} \cdot \boldsymbol{r}_p^t)$. Thus, if one assumes that the polarization of this field and/or that of the reference field are properly adjusted, the phase of the output fibre field can be determined. In this case, the measured phase is actually the *same* as that of the probed wave field (bar a constant difference). One can safely assume that the amplitude-coupling matrix $\boldsymbol{H}(\boldsymbol{k}_p)$ is a continuous vector function arriving thereby at the main conclusion: the phase-sensitive SNOM allows one to map the amplitude and the phase of an optical field provided that it has sufficiently narrow polarization range and spatial frequency spectrum. Thus, this technique has been successfully used to image the fields of individual evanescent waves [43] and waveguide modes (of the same polarization) with similar propagation constants. [24] The situation with imaging of a standing evanescent wave formed by counter-propagating waves [44] is somewhat more complicated. Still, in the case of TE polarization and a symmetric detection conFiguration, the output signal field replicates faithfully the probed field because $\boldsymbol{H}(\boldsymbol{\beta}) = \boldsymbol{H}(-\boldsymbol{\beta})$ [26, 27].

Finally, we would like to warn against using this technique in cases where the polarization spectrum of the probed field is not precisely known, e.g., when imaging the field scattered by subwavelength-sized surface features. Light scattering by nanostructures gives rise to *differently* polarized wave components, so that there is a great risk that the observed features, e.g., phase singularities, would turn out to be an artifact of the imaging technique used. The presented description indicates also a simple way to check against such a possibility, viz., a true phase image should be stable (within an additive constant) with respect to perturbations (e.g., bending and twisting) of the fibre used, if the perturbation is held constant during the image acquisition. Such a perturbation can only influence the amplitude of the detected signal and change proportionally the amplitude image. The treatment of image formation in the collection SNOM presented in this section should help to better exploit the possibilities offered by the SNOM technique for mapping the phase and the amplitude of optical near fields.

3. Near-field intensity detection

Material presented in this section is based on the results obtained at telecom wavelengths with the *intensity* detection SNOM conFiguration [35-37], including recent results on the PhCW phase and group velocity characterization [45]. The experimental setup consisted of a collection SNOM with an uncoated fibre tip used as a probe [46] and an arrangement for launching tuneable (1500 – 1630 nm) TE/TM-polarized (the electric field is perpendicular/parallel to the sample surface) radiation into the input ridge waveguide by positioning a tapered-lensed polarization-maintaining single-mode fibre. The adjustment of the in-coupling fibre with respect to the sample facet was accomplished when monitoring the light propagation along the sample surface with help of a far-field microscopic arrangement [36]. Following the fibre adjustment, the intensity distribution near

the sample surface was probed with an uncoated sharp fibre tip of the SNOM apparatus [Fig. 2(a)]. The tip was scanned along the sample surface at a constant distance of a few nanometers maintained by shear force feedback. Near-field radiation scattered by the tip was partially collected by the fibre itself and propagated in the form of the fibre modes towards the other end of the fibre, where it was detected by an InGaAs photoreceiver with a sensitivity of the order of femtowatts.

All investigated samples were fabricated on silicon-on-insulator (SOI) wafers, consisting of a perforated $SiO_2/Si/SiO_2$ trilayer film (cladding/core/buffer thickness ~0.1/0.3/1 μm) formed on a Si substrate [47]. Holes were arranged in triangular periodic arrays with different parameters and single rows of missing holes defined the PhCWs along ΓM direction of the irreducible Brillouin zone of the lattice [1]. Electron-beam lithography was employed when fabricating these samples to produce hole patterns in a resist layer deposited on a SOI wafer. The patterned resist served as a mask in the process of reactive ion etching (RIE) resulting in the corresponding pattern of holes formed in the Si layer. After removal of the resist, the pattern was further transferred onto the SiO_2 layer by RIE, using the patterned Si layer as a mask. Finally, samples were thermally oxidized in order to grow a thin SiO_2 layer on top of the Si layer and on the inner walls of the air holes, because the silica top cladding increases the vertical symmetry of the structures and smoothens out surface roughness of the structures [47]. Three different PhCW structures were fabricated and investigated: sample A having the period $\Lambda \cong 410$ nm and hole diameter $\cong 200$ nm [35-37], and samples N1 and N2 having the same period of 428 nm but different hole diameters, viz., 325 and 350 nm, correspondingly [45]. The samples contained central PhC areas (with PhCW regions of different lengths) connected to tapered access ridge waveguides outside the PhC areas as shown in Fig. 2(b). Ridge waveguides, gradually tapered from a width of ~ 4 μm at the sample facet to ~ 1μm at the PhC interface, are used to route the radiation to and from the PhCWs.

Typical topographical and near-field optical images obtained for the PhCW (sample N1) at the wavelength of 1520 nm (TM polarization) are shown in Fig. 3 along with the microscope image of a tapered fibre positioned against an access ridge waveguide. On the topographical image [see Fig. 3(b)], the input and output ridge waveguides are clearly seen. One can also easily recognize the PBG structure on the topographical image, but the pattern of holes that forms the PhCW following by input and output waveguides is not discernible, because the scanning parameters were not optimised with respect to the topographical imaging. The near-field optical image [Fig. 3(c)] exhibits several features appearing also on the images obtained with other PhCWs and at other wavelengths. The light propagating along the input ridge waveguide and further in the PhCW and along the output waveguide is clearly seen, as well as the light scattering at the junctions between the PhCW and ridge waveguides. The light scattering at junctions results in scattered field components propagating (in air) away from the sample surface. These propagating components are detected with the SNOM fibre tip much more efficiently than the evanescent field components [26], e.g., associated with the PhCW and ridge waveguides modes, resulting in the image contrast distortion [35-37]. It should be also noted that the signal does not go to zero outside the PhCW indicating the presence of homogeneous background at the level of ~ 10 % compared to the maximum signal. Finally, it is seen that the recorded intensity distribution is well confined (to the line of missing holes defining the PhCW) in the transverse direction and exhibiting a somewhat irregular pattern in the propagation direction.

3.1. Mode characterization

SNOM images obtained with high resolution revealed that the intensity distributions along the PhCWs are quasi-periodic and wavelength dependent (Fig. 4). We have related this remarkable feature (also found in the experiments on SNOM imaging of conventional waveguides [23]) to the

interference between fibre modes excited by the SNOM fibre tip interacting with both PhCW mode evanescent fields and weak optical fields forming a quasi-homogeneous background [36]. All plane wave components of the *total* probed field contribute linearly (though with different efficiency decreasing rapidly for high spatial frequencies) to the amplitude of the fibre modes propagating toward a photodetector. Therefore, in the SNOM imaging of the PhCW modes, especially those with large effective indexes, even weak scattered optical fields caused by material inhomogeneities and fabrication defects can noticeably contribute to the detected signal. This contribution being coherent and most strong from the optical fields with small wave-vector projections results in an interference pattern superimposed on the image formed by a waveguide mode. Such an interference pattern is somewhat irregular due to different contributing plane wave components, exhibiting the interference fringes corresponding to the optical field with zero wave vector projection (propagating away from the surface) i.e., to the homogeneous coherent background.

In the case of the PhCW oriented along the x-axis, the field probed by the SNOM above the sample surface and along the PhCW can be approximated as follows [36]:

$$E_d(x,z) = B + \sum_m u_m^0 \exp\left[-z\sqrt{(\beta+mK)^2 - k_0^2}\right]\exp[i(\beta+mK)x] \quad , \qquad (3)$$

where $K = 2\pi/\Lambda$, $m = 0, \pm1, \pm2, \ldots$, the z axis is perpendicular to the sample surface ($z = 0$) pointing to the air side, B represents a homogeneous background field, $k_0 = 2\pi/\lambda$ is the wave number in air, u_m^0 is the amplitude of the main electric field component of the PhCW mode having the propagation constant β, Λ is the PhC lattice constant. It is also assumed that all Bloch components are evanescent. Each of the field components described in Eq. (3) contribute to the amplitude of the fibre mode amplitude, which is actually detected. However, the coupling efficiency decreases drastically with the increase of the wave vector surface projection $|\beta + mK|$ as mentioned above. This dependency can be qualitatively explained by the circumstance that the effective detecting

centre of a SNOM probe fibre is situated at some distance (up to 500 nm) from the tip extremity [48, 49], so that the *evanescent* fields are always probed at a nonzero distance from the surface. Keeping only the leading terms, the signal detected (along the PhCW) at the tip-surface distance z reads

$$S(x,z) \propto C(z) + 2h(0)Bh(\beta)u_0^0 \exp(-z/d_0)\cos(\beta x) + \\ + 2h(0)Bh(K-\beta)u_{-1}^0 \exp(-z/d_1)\cos[(K-\beta)x] + 2h(\beta)u_0^0 h(K-\beta)u_{-1}^0 \exp(-z/d_2)\cos(Kx)\,, \quad (4)$$

where $C(z)$ denotes the level of signal background, whose distance dependence is due to the averaged intensity of the evanescent waves, $h(k)$ is the detection efficiency of the field component having the magnitude k of wave vector projection on the surface plane, and the penetration depths are given by [Eq. (3)]

$$d_0 = (\beta^2 - k_0^2)^{-0.5}\,, \qquad d_1 = \left[(K-\beta)^2 - k_0^2\right]^{-0.5}\,, \qquad d_2 = \frac{d_0\, d_1}{d_0 + d_1}\,. \quad (5)$$

It is expected that $h(0) >> h(\beta) > h(K - \beta)$ for the aforementioned reasons and, thereby, the signal harmonics having spatial frequencies β and $K - \beta$ would dominate the spectrum [Eq. (4)].

This consideration can be generalized for the case of two PhCW modes having the propagation constants β_1 and β_2 [37]. In this case, the dominating signal harmonics would be those with spatial frequencies β_1, β_2, $K - \beta_1$, and $K - \beta_2$. The occurrence of several PhCW modes might be caused by the excitation of different depth modes of the input ridge waveguide. One can also expect that some of the modes would be actually *index*-guided modes that would not exhibit well pronounced PBG properties.

The typical spatial frequency spectrum of the optical signal variations along the PhCW measured at the surface of sample A is shown in Fig. 5 for the light wavelength of 1540 nm. The spectrum features several peaks that can be assigned, in agreement with the arguments given in the previous section, to the spatial frequencies of two PhCW modes with the propagation constants β_1

and β_2. The lattice constant of 410 nm of our PC was obtained from images made by a calibrated scanning electron microscope and corroborated with SNOM topographical images [36]. The PhCW mode propagation constants β_1 and β_2 were fitted to the experimental spectrum so that the frequencies $K - \beta_1$ and $K - \beta_2$ would also fit to the corresponding peaks as shown in Fig. 5. One can further see that the spectrum structure, being well defined at low spatial frequencies, is more complicated around the frequency K of the lattice constant. Such a structure might be related to the PhCW modes reflected by the PhCW-ridge waveguide interface and the output edge of the sample and/or to the nonlinear response of the photoreceiver used for optical signal detection [36]. Considering current observations, we should remark that the mode with β_1 is most probably the main (true) PhCW mode, whereas the mode with β_2 is only index-guided and excited due the multi-mode light propagation in the input ridge waveguide. The above fitting procedure was carried out (with sample A) for other wavelengths in the spectrum range of 1520 1570 nm resulting in the first dispersion curve measured with the SNOM [37].

Dispersion of light propagation along the PhCW was studied in most detail for sample N1 [45]. The fitting procedure described above was accomplished for both polarizations in the whole wavelength range available (1500 – 1630 nm). Thus determined the propagation constant of the true PhCW mode was found to be varying faster with the light wavelength than that of free propagating (in air) radiation. For example, in the case of TE polarization, the ratio Λ/λ_{PhCW} changed from 0.33 to 0.41 when the ratio Λ/λ varied from 0.28 to 0.29 [45]. Such dispersion is actually expected for the PhCW mode in SOI PBG structures [50]. Considering the wavelength dependence of the propagation constant determined from the corresponding spatial spectra, we calculated the phase and group velocities for TM- and TE-polarized PhCW modes in the wavelength range of 1500-1610 nm (Fig. 6). It is clearly seen that the group velocity rapidly decreases, reaching the values of ~ $0.11c$ at the light wavelength of 1610 nm for TM polarization and ~ $0.035c$ at the wavelength of

1522 nm for TE polarization, as the wavelength increases towards the PBG edge. At the same time, the phase velocity does increase though relatively slow so that the PhCW mode constant becomes closer to the light line in air for longer wavelengths. It should be mentioned that this behaviour of the group velocity is in agreement with the recent results obtained with different techniques [18, 39]. Finally, it should be mentioned that the experimentally established large dispersion and significant reduction in the group velocity, which are directly related to the tight confinement and strong Bragg scattering in the PhCW, were also corroborated with the theoretical dispersion curves calculated with the 3D finite-difference time-domain (FDTD) method [45].

3.2. Loss measurements

Light propagation along the PhCWs of samples N1 and N2 and the associated loss were studied in great detail for both polarizations in the whole wavelength range available (1500 – 1630 nm) using the corresponding high-quality and -resolution SNOM images obtained [45]. For TM polarization, the efficient guiding along the PhCW was observed in the whole wavelength range (Fig. 7) for both samples, a feature that suggests the absence of PBG and pure effective-refractive-index guiding of TM mode (similar to the conventional dielectric waveguiding). At the same time, for TE-polarization, the efficient guiding was limited to the wavelengths shorter than 1522 or 1570 nm for the PhCW with the filling factor of 0.76 (sample N1) or 0.82 (sample N2), respectively. For longer wavelengths, we observed drastic and rapid deterioration of the waveguiding and PhCW mode confinement, ending up with the complete disappearance of the PhCW mode once the wavelength exceeded the cutoff value by merely 2 nm (Fig. 8). Such a critical wavelength dependence of the PhCW guiding for TE polarization can be considered as a clear evidence of the well-defined PBG effect in the structure. It should be noted that the long-wavelength PBG edge was found shifting

towards longer wavelengths with the increase of the filling factor, a circumstance that emphasizes the fact that the filling factor is an important design parameter for PhCWs.

Using the SNOM images obtained at different wavelengths (similar to those shown in Figs. 7 and 8) one can directly determine the PhCW mode propagation loss and its dispersion. Variations in the detected signal along the PhCW axis, which can be used to determine the mode propagation constant (see the previous subsection), made the precise evaluation of the propagation loss rather difficult. In order to circumvent this problem, we have determined the propagation loss by averaging over 11 profiles of the (~ 25-μm-long) intensity distributions that were cut along the PhCW axis and finding the slopes of the best linear fits to the corresponding average cross sections. This procedure was carried out for different wavelength, and the obtained results were recalculated as transmission through the 10-μm-long PhCW of sample N1 and the 40-μm-long PhCW of sample N2. The latter were compared with the transmission measurements conducted with the same samples using the conventional approach of measuring the transmission spectra for PhCWs of different lengths (Fig. 9).

This (direct) comparison between the experimental transmission spectra and the data obtained from the corresponding SNOM images showed rather good correspondence in the wavelength ranges of mode guiding as seen from the SNOM images. At the same time, it became apparent that the conventional technique of characterization might turn out to be somewhat misleading as it does not provide a clear evidence of the PhCW mode cutoff behaviour, showing instead a gradual decrease in the transmission. One can also notice that the transmission measurements tend to overestimate the propagation loss near the PBG edge (Fig. 9) probably because the coupling between the access ridge waveguides and the PhCWs becomes unstable (due to a drastic increase in the FWHM of PhCW modes). This means in turn that large propagation losses usually reported for the PhCW modes close to the PBG edges (these modes are interesting due to high dispersion and

low group velocities) might be a result of overestimation. It should be borne in mind that the difference in spectral resolution of measurements performed using the tuneable laser and LED might also have influenced the transmission curves obtained, e.g., by smoothening the transmission curve measured with the LED.

3.3. Y-splitters

SNOM intensity detection has also been used to characterize more complicated PhCW structures, such as gradual and sharp bends [37], diffraction grating couplers [51], Y-splitters [52] and directional couplers [53]. Terminating a review of the results obtained with the SNOM intensity detection, we consider in this section the characterization of PhCW-based Y-splitters [52]. Schematic of the experimental arrangement is shown in Fig. 10 along with a scanning electron micrograph of a hole arrangement in the studied sample. Holes were arranged in a triangular array (lattice constant $\Lambda \cong 430$ nm, hole diameter $\cong 260$ nm) and single row of missing holes defined the PhCWs in the otherwise perfect PhC. The sample contained a central PhC area connected to tapered access ridge waveguides outside the PhC area [Fig. 10(b)]. Ridge waveguides, gradually tapered from a width of ~ 4 μm at the sample facet to ~ 1μm at the PhC interface, were employed to route the light to and from the PhCWs.

Typical topographical and near-field optical images obtained for the Y-splitter at the wavelength of 1550 nm for TM polarization are shown in Fig. 11. On the topographical image [Fig. 11(a)], the input and output ridge waveguides are clearly seen. It is rather problematic to recognize the PBG structure on the topographical image, because the scanning parameters were not optimised with respect to the topographical imaging. On the near-field optical image [Fig. 11(b)], one observes light propagating along the input and output ridge waveguides as well as strong light scattering from the PhC area originating at the junctions between the PhCWs and ridge input/output

waveguides. It should be borne in mind that the scattered (out of the surface plane) and propagating field components are detected with the SNOM fibre tip much more efficiently than the evanescent field components associated with the PhCW mode fields (as elaborated in section 3.1). One should take this circumstance into account when designing the sample with PhCW structures and, for example, introduce longer pieces of straight PhCWs connecting a region of interest (with a splitter, coupler, etc) with ridge waveguides.

The features in light propagation inside the same PhCW structure and along output ridge waveguides became better visible in the high-resolution optical images recorded separately with different sensitivities (Fig. 12). However, a rather small size of the PhC region (7×7 μm^2) containing the investigated Y-splitter and light scattering at the junctions between PhCWs and ridge waveguides lead to the contrast distortion in the SNOM optical images recorded in the Y-splitter area. This circumstance impedes observation of the PhCW mode intensity distributions and makes a direct treatment of the images obtained rather complicated. One can still characterize the splitting efficiency and the loss incurred by recording SNOM images of the input and output ridge waveguides. Thus, for TM polarization, we observed the efficient guiding along the output RWs with nearly 50/50 splitting efficiency at the wavelengths close to 1425 and 1550 nm [see, e.g., Fig. 12(c)], whereas the splitting at other wavelengths was noticeably unequal [see, e.g., Fig. 12(e)].

The corresponding SNOM images obtained at the same wavelengths inside the PhC area [Figs. 12(d) and 12(f)] show several features appearing also at other wavelengths, such as intensity variations along the propagation direction and relatively strong light scattering at the fork and bend PhCW regions. It was found that the intensity distributions were symmetric with respect to the line of input PhCW for the wavelengths, at which the splitting efficiency was found equal, and vice versa [cf., Figs. 12 (d, f) and Figs. 12 (c, e)]. Note that the bright spot observed at the top of Fig. 12(f) (in between the output ridge waveguides) was most probably caused by light propagating

through the periodic structure in the forward direction and scattering at the boundary of the PhC area. A possible explanation of the observed features might be related to the fabrication quality of the PhCW structure. It is clear that even small deviations of the corresponding hole structure from the perfectly symmetric one (e.g. cavities or other lattice defects in the fork and bend regions of the splitter) may strongly influence the process of waveguiding and splitting of PhCW modes. Rather complicated field intensity distributions observed with the PhC area are believed to be originated form the excitation of such bend cavities at different wavelengths, a fact that results in the detected asymmetrical intensity distributions.

Similar features have also been found for TE polarization of input radiation except for the fact that the efficient PhCW guiding was observed only within the wavelength range of 1545-1555 nm [52]. Such a remarkable difference between PCW guiding in two polarization conFigurations observed in this case and with straight PhCWs (section 3.2) is related to the fact that a triangular pattern of holes can provide the PBG only for TE polarization, a circumstance that reveals pure effective-refractive-index guiding of TM mode (similar to the conventional dielectric waveguiding) [54]. This feature accounts for broadband transmission of TM polarization and wavelength limited (within the PBG) transmission of TE polarization that was observed with this sample as well as with those considered in the previous section.

4. Near-field amplitude detection

Material presented in this section is based on the results obtained at visible and near-infrared wavelengths with the *amplitude* detection SNOM conFiguration [40a, 40b, 55], including the most recent results on local probing of Bloch harmonics [40] and real-space pulse tracking that allowed us a direct access to the PCW phase and group velocity characterization [39].

Two types of photonic crystal structures are used in the following section. The first is a one-dimensional hole array fabricated in a conventional ridge Si_3N_4 waveguide. The second is a so-called W3 waveguide in a hexagonal, two-dimensional photonic crystal consisting of air holes in a Si background. The basis for the first structure is a Si_3N_4 ridge waveguide. A 55 nm layer of Si_3N_4 is deposited with low-pressure chemical vapour deposition on a 3 μm SiO_2 layer. Conventional contact lithography is used to define a 1.4 μm wide waveguide which is fabricated by etching a 11 nm ridge with reactive ion etching. A periodic array of 15 air rods is subsequently milled into the structure with a focused ion beam [56]. The periodicity of the air rods is 220 nm and the air rod diameter is 110 nm. The W3 PhCWs were fabricated on a silicon-on-insulator wafer, which consists of a 220 nm thick Si layer on top of a 1 μm SiO_2 cladding layer [57]. The holes are arranged in a hexagonal pattern. Two crystals are fabricated, one with a period of 400 nm and one with a period of 460 nm. The hole radius is 130 nm. Three missing rows of holes form the W3 waveguide.

In all near-field optical experiments coated probes were used. The basis for the probes is a single mode optical fibre which is melted with a CO_2 laser and pulled to a very sharp tip, radius of curvature of the end face < 50 nm. It is subsequently coated with Al and an aperture is defined with focused ion beam milling [58]. The reason for using coated probes is that it strongly reduces the amount of background signal that may arise from scattering from the photonic crystal structures [59].

4.1. Local phase detection in photonic crystal structures

For the local detection of phase inside photonic crystal structures the collection mode SNOM setup has to be expanded. The light incident on the structure is split in two branches: a reference branch with a constant, albeit accurately adjustable, optical path length and the signal branch which is formed by the original collection mode SNOM including the optical path through the photonic crystal structure. The light in the reference branch can be acousto-optically modulated to allow for

heterodyne detection after both branches have been interferometrically mixed [23a, 60]. The heterodyne detection allows the detection of 2 signals separately that are proportional to: $A(x,y)\cos\varphi(x,y)$ and $A(x,y)\sin\varphi(x,y)$, where $A(x,y)$ is the amplitude of the collected light at sample position (x,y) and $\varphi(x,y)$ is the phase difference between the reference and the signal branch for the same probe position. Simple mathematics suffices to separate the amplitude from the phase information. When care is taken to minimize phase drift in the instrument due to thermal fluctuations and air flows, the phase difference is fully determined by the change in optical path length in the sample as the probe is scanned across it. Thus the phase evolution and therefore the phase velocity of the light as it propagates through the structure become directly accessible.

A direct consequence of this is that when the optical frequency is known (incident laser), the propagation constant (or wave-vector) and conversely the effective refractive index of the structure can be measured unambiguously. Figure 13 depicts a phase-sensitive measurement of light propagating around a photonic crystal structure consisting of a periodic arrangement of air holes fabricated in a conventional ridge waveguide. Light (λ_0=632.8 nm in air) enters the structure from the top of the image. Figure 13a, depicts the topography of the structure as measured with the scanning near-field probe as it is kept at a constant separation from the sample surface. Figure 13b shows the measured $\cos\varphi(x,y)$ of the light around the structure. The plane wave, consistent with the fundamental mode of the ridge waveguide, is incident on the periodic hole structure has a wavelength inside the structure of 439(4) nm corresponding to an effective refractive index n_{eff} = 1.441(0.014), the straight wave-fronts are affected by the holes. Significantly, at the location of the holes the local wavelength is found to be 411(4) nm corresponding to an effective refractive index that is 6% higher than that of the fundamental mode of the ridge waveguide. The fact that the index is higher, despite the fact that air holes are introduced into the background material, is attributed to the anomalous dispersion caused by the periodicity of the structure.

Figure 14a shows the measured $A(x,y)\cos\varphi(x,y)$ of light propagating for a larger area around the same structure. The light is again incident from the top of the image. The colour-coding of the image is such that bright and dark indicate large positive and negative values, respectively. These correspond to areas where the field amplitude is high. Conversely, intermediate grey levels indicate low amplitudes: e.g., the amplitude near the left and right borders of the image are near zero. It is clear from the image that many scattering phenomena occur and that the fields around the structure are formed by the interference between the incoming, the scattered and the transmitted light. Figure 14b shows the intensity of a two-dimensional Fourier transform of the optical information contained in Fig. 14a. Two important spatial frequency regions are pronounced, corresponding to the directions along the ridge waveguide with both an upward and a downward direction. Two concentric rings can also be distinguished. The details of the scattering can be unravelled through Fourier filtering. Thus, the complex pattern depicted in Fig. 14b is split into the 3 most important contributions, shown in Figs. 14d,f&h. 14d shows the spatial frequencies of the dominant peaks in of the spectrum Fig. 14b. Inverse transformation of Fig.14d recovers the plane wave which is omnipresent in the entire image, which has a wavelength of 439(4) nm and corresponds to an effective index $n_{\text{eff}} = 1.441(0.014)$. In Figs. 14f&h two other strong features were selected. The images of the inverse transformations Figs.14e&g, respectively, reveal plane waves scattered under discrete angles away from the periodic air rod structure. In Fig. 14e we find an angle of 15° with respect to the direction of the fundamental waveguide mode. The spatial frequency corresponds to a wavelength of 527 nm and thus an effective index of 1.20. Figure 14g reveals plane waves with an effective index of 0.90, corresponding to a wavelength of 703 nm, which propagate under an angle of 21.5° with respect to the ridge waveguide. We find a reasonable correspondence of the measured refractive indices with those of leaky slab modes of the layer package: TE_{07}: $n_{\text{eff}} = 1.233$ and TE_{10}: $n_{\text{eff}} = 0.98$.

4.2. Local probing of Bloch harmonics

Local phase-sensitive near-field measurements can be exploited to investigate photonic crystal waveguides in great detail. In particular, the capability to measure all the spatial frequencies inside the waveguide is powerful as it can unravel the band structure of the optical modes inside the structure. The potential of the technique is highlighted with measurements on to model structures: a W3 (three rows of air holes missing) waveguide in a silicon-on-insulator (SOI) layer package studied with near infrared and a W1 waveguide in a freestanding Si_3N_4 membrane studied with visible light.

The W3 structure is displayed in Fig. 15b only contains 32 periods whereas the real structure under investigation contains 256. Figure 15b depicts all the relevant details of the structure including the access and exit ridge waveguides. TE-polarized light from a tunable femtosecond laser is coupled into the structure with an objective lens.

Figure 16 depicts a typical phase-sensitive near-field measurement on the W3 PhCW. The topography that is measured by scanning the near-field probe across the sample surface while keeping the probe-sample separation constant is shown in Fig. 16a. The main features of the structure are visible, e.g., the access and exit ridge waveguides on the left and right of the image, respectively. In the centre of the image the hole pattern of the photonic crystal can be distinguished. The raw optical data of one of the channels of the lock-in-amplifier, which is proportional to the local optical amplitude times the cosine of the optical phase, is depicted in Fig. 16b. The grey scale maps negative and positive signals to dark and bright grey levels, respectively. The combination of spatial amplitude and phase information makes that all the relevant spatial frequencies of the light in the photonic crystal structure for the given optical frequency are contained in the image. It is clear that a large range of spatial frequencies is visible in the image. Figure 16c depicts the amplitude information only. From this image it is apparent that for the optical frequency used,

several modes can be simultaneously excited. The differences in group velocity of the modes results in the break up of the femtosecond pulse in the PhCW.

A spatial Fourier transform of the optical information (amplitude time cosine of the phase) along the x-direction in Fig. 16b yields the spectrum $F(|k_x|)$ of the magnitude of the spatial frequencies ($|k_x|$) for ω = 0.369. This Fourier analysis is repeated for measurements with different incident wavelengths ranging from 1180 nm to 1345 nm, where the wavelength is increased in steps of 5 nm. In this way all the excited spatial frequencies for the optical frequencies in the range ω = 0.342 to ω = 0.390 are determined in frequency steps of ω ~ 0.002. This allows the measured band structure of the PhCW to be constructed. Figure 17 depicts a greyscale representation of the measured band structure. The vertical axis depicts the optical frequency ω and the horizontal axis corresponds to the spatial frequency. The greyscale levels indicate the relative amplitude of the spatial frequencies present in the PhCW. A logarithmic greyscale was used to depict the full range of relative amplitudes in the PhCW.

We observe not only information in the first Brillouin zone (BZ), but also in higher (up to 4) BZ's. This proves that Bloch modes are excited in the waveguide, as they can be decomposed into a sum of plane waves or Bloch harmonics with wave-vectors separated by 2π/a, with a the lattice spacing. The simultaneous observation of positive and negative slopes in the band structure results from the fact that the relation between optical frequency ω and the magnitude of the spatial frequency is measured. The bands of negative slopes, in this case, do not belong to Bloch modes with a negative group velocity, rather they belong to Bloch harmonics with a negative wave-vector [39, 40b]. Through a direct model-independent measurement of the photonic band structure and the mapping of many Bloch harmonics inside the photonic crystal structure phase-sensitive near-field microscopy is an ideal technique for testing theoretical models and investigating the intricacies of light propagation in photonic crystals.

4.3. Real-space pulse tracking

As was already alluded to in the previous section, the heterodyne interferometric SNOM can also be used to study the dynamic properties of PhCW's when it is used in conjunction with ultrafast pulses. When pulses are used in the phase-sensitive microscope, interference is only detected if the pulses propagating through the reference and signal branches, respectively, have temporal overlap when they arrive at the mixing point. This means that when an extra optical delay is added to the reference branch, interference will be detected further along the PhCW: in effect the optical delay in the reference branch sets a reference time [24]. In actual fact the measured signal as a function of the probe position for a given reference time is a complex cross-correlation that also contains the dispersive properties of the sample structure. For a more detailed description of the actual optical signal measured in a pulse tracking experiment, the reader is referred to refs61&62.

Figure 18 depicts a pulse tracking measurement in a W3 PhCW. Ultrashort transform limited pulses (FWHM 120 ± 10 fs, $\Delta\omega \approx 0.02$) where launched into the access waveguide with a wavelength of 1245 nm in air. The measured topography is presented in Fig. 18a. Figures 18b through g show the measured amplitude signal for increasing reference time (time step = 400 fs). In Fig. 18b at $t = 0$ fs the pulse has just reached the PhCW. In the next frames a pulse break up is immediately obvious: the pulse excites various modes each propagating with a different velocity. It is visible that the different modes also have different lateral mode profiles. For example, the slowest mode penetrates further into the 2D photonic crystal than the fastest modes, which has most of its amplitude in the waveguide only.

The different modes not only differ in their mode profile, also their wavevector is different (see above). The time evolution of the different modes can therefore be extracted through a Fourier filtering of the combined amplitude and phase information that allows the propagation of the different Bloch modes to be separated. Subsequently, the position of the "centre of mass" (CoM) as

a function of time can be determined for the different Bloch modes. Provided that the pulses are roughly Gaussian and retain their shape while propagating through the PhCW, the speed of the CoM is an unambiguous measure for the group velocity of the Bloch mode. The positions of the CoM for these Bloch modes are given in Fig. 18h. The slope in this graph yields group velocities ranging from $(0.121 \pm 0.001) \times c$ to $(0.243 \pm 0.001) \times c$, where c is the speed of light in vacuum. Thus, for $\omega = 0.369$ group delays are found ranging from 4 to roughly 8. Not all Bloch modes found for $\omega = 0.369$ could be analysed in this fashion as for some group velocity dispersion (GVD) resulted in large distortions of the measured signal. For $\omega = 0.369$ was found for a mode with $k = 0.797$ the strongest GVD was found: 3×10^5 ps^2/km. This observed GVD is roughly 5 orders of magnitude larger than that of a conventional single-mode fibre.

When extrapolating the graphs in Fig. 18h another important discovery is made: the various Bloch modes are not excited at the same time. The observed time delay can be as large as 500 fs. The time lags are probably caused by the fact that multiple modes in the access waveguide couple to multiple modes in the PhCW. Similar time lags could never have been observed in conventional 'time-of-flight' (TOF) measurements of pulse propagation through PhCW's, in which the photonic crystal structure is treated as a "black box". For TOF measurements on very short structures a time lag of 500 fs could result in large errors of the determined group velocity.

As mentioned in the previous section, the measured phase-sensitive information can be used to construct the photonic band structure of the PhCW. Figure 19a shows the measured band structure of this W3 waveguide. The slopes in this measured band structure for an optical frequency $\omega = 0.369$ corresponds to the measured group velocities determined from the time-resolved pulse propagation measurements. In the band structure we are able to identify a flat part of the dispersion curve close to the Brillouin zone boundary (indicated by the arrow) which is indicative of a localized and/or slow mode in the waveguide. Figure 20 presents a pulse tracking measurement for

this flat band ($\omega = 0.305$), with HJ-S-4a the measured topography. Figures 20b-k show the measured amplitude signals as the reference time is increased in steps of 600 ± 1 fs. Several dynamic phenomena are observed. Firstly, in the first 4 frames we observe a first order mode propagating through the PhCW. But secondly, in the wake of this relatively fast pulse striking effects are visible. Fascinatingly, we observe a localized and seemingly stationary optical pattern in the first 25 μm of the W3 PhCW. The localized light field persists for very long times. Its pattern is reminiscent of the patterns associated with mini-stop gaps [63,64]. Despite the fact that the PhCW is an open structure without any (obvious) mirrors of reflectors, the pattern persists for more than 3.6 ps. A trapping time can be related to a quality factor Q of a resonator by $Q = \omega\tau$, where τ is the trapping time. A trapping time at this frequency is equivalent to $Q \cong 6 \times 10^3$. After 3.6 ps the shape of the optical patters changes, but optical fields with wave-vectors right on the boundary of the Brillouin zone are still present in the PhCW after more than 5 ps. Movement of the localized pattern is hardly discernible between 1.2 and 4.2 ps. Given the experimental parameters only an upper boundary can be given for the speed of the light field: the speed is at most c/1000. The nature of this localized light field will be the subject of further investigation. Note that it is not excited at the very start of the PhCW. A pulse propagating at c/1000 would take many nanoseconds to arrive at the location where we observe it. This means that the light field is not simply a very slow pulse propagating through the structure. The shape of the pattern also needs to be taken into account when explaining this phenomenon. The slow amplitude modulation which is visible and which results in the three-lobed pattern suggests that several modes with slightly differing wavevectors interfere to form the pattern.

Our observation of this ultraslow, localized light pattern highlights the power of local (time-resolved) investigations in photonic crystal structures, because these observations could never have been made with conventional input-output measurements.

5. Conclusions

In this review, we considered various aspects of PCW characterization by making use of SNOM techniques. We have shown how the intensity detection can be used to map mode profiles determine losses locally, gain insight into the Bloch nature of the propagating light and investigate more complex photonic crystal-based structures. We have also demonstrated that the phase-sensitive detection allows the Bloch nature to be investigated in more detail as all the Bloch harmonics belonging to a single Bloch mode can be unravelled. Time-resolved SNOM measurements (pulse tracking measurements) allow pulse propagation to be visualized and phase- and group velocity to be determined independently with the need for modelling.

Using the SNOM in collection mode, we have imaged the propagation of light at telecommunication wavelengths along straight silicon-on-insulator PhCWs (with different filling factors) formed by removing a single row of holes in the triangular 410-nm-period lattice. High quality SNOM images of PhCWs excited in the wavelength range of 1500-1630 nm have been obtained and analyzed to determine the PhCW characteristics for TE and TM polarizations. Thus, we have analyzed light intensity variations along PhCWs measured with the SNOM and related these variations to Bloch components of the PhCW mode. Using a phenomenological description of the SNOM imaging and assuming the presence of a quasi-homogeneous background field, we have identified in spatial frequency spectra of the intensity variations of the corresponding Bloch harmonics and determined (for both polarizations) the dispersion of the PCW mode propagation constant and, thereby, the mode group and phase velocities. The efficient guiding (for both samples) of the TM-polarized radiation was observed in the whole range of laser tunability. At the same time, for TE-polarization, the efficient guiding was limited to the wavelengths shorter than 1552 or 1570

nm for the PCW with the filling factor of 0.76 or 0.82, respectively. For longer wavelengths, we have observed drastic and rapid deterioration of the waveguiding and PCW mode confinement, once the wavelength exceeded the cutoff value by merely 2 nm. Such a critical wavelength dependence of the PCW guiding (for TE polarization) is, in our opinion, a clear evidence of the well-defined PBG effect in the structure. Using averaged cross sections of the intensity distributions along the PCW axis, the propagation loss has been evaluated and found to be in good agreement with the corresponding transmission spectra.

Phase-sensitive measurements have been presented that show how SNOM can be used to investigate local scattering phenomena around finite sized periodic structure. The phase-sensitivity was exploited to separate the various scattered modes. Phase-sensitive measurements of Bloch modes allowed the direct visualization of these modes and enabled the determination of the spatial frequency spectrum without requiring a background field. Note that, by determining the spatial frequencies in the PhCW for different optical frequencies, the full photonic band structure can be measured spanning many Brillouin zones. Time-resolved measurements allow a model-independent determination of the group velocity of the different Bloch modes. These local measurements do not suffer from integrating all propagation effects through the entire structure, including access and exit waveguides, as the group velocity is measured locally. Importantly, it was shown that a time lag may exist when exciting a multimode PhCW from a multimode access waveguide. Such a time lag might greatly influence group velocity measurements on short structures. For a specific optical frequency an ultraslow localized light field was discovered.

We believe that the results presented in this work can help in designing further, more detailed and accurate, SNOM investigations of PhCWs and, in general, PhC structures. The accurate PhCW characterization is particularly important since rigorous calculations of the properties of PhCW components are extremely difficult and time consuming. The SNOM imaging can be used not only

to quantitatively characterize properties of fabricated PhCWs (mode profiles, propagation constants including loss and the dispersion) and PhC structures (evaluation of loss and identification of loss channels) and thereby optimize their performance, but also to unveil many intriguing scattering phenomena occurring in PhCs that may remain hidden to far-field or input-output measurements.

6. Acknowledgements

Contributions of Valentyn Volkov, Peter Borel and Martin Kristensen in obtaining results reviewed in Section 3 are greatly appreciated. Rob Engelen, Henkjan Gersen, Eliane Flück, Tim Karle, Wim Bogearts, Jeroen Korterik, Bert Otter, Niek van Hulst and Thomas Krauss are gratefully acknowledged for their contributions to Section 4. One of the authors (SIB) acknowledges the support from the national frame programme “Planar Integrated Photonic Band Gap Elements (PIPE)” financed by the Danish Technical Research Council, contract No. 26-03-0158. Part of this work is part of the research program of the “Stichting voor Fundamenteel Onderzoek der Materie (FOM)”, which is financially supported by the “Nederlandse organisatie voor Wetenschappelijk Onderzoek (NWO)". LK acknowledges financial support for the Network of Excellence PHOREMOST.

References

[1] Joannopoulos J D, Meade R D and Winn J N 1995 *Photonic Crystals* (Princeton, NJ: Princeton University Press)

[2] Bykov V P 1993 *Radiation of atoms in a resonant environment* (Singapore: World Scientific)

[3] Soukoulis C M, ed. 2001 *Photonic Crystals and Light Localization in the 21st Century* (Dordrecht: Kluwer)

[4] Krauss T F and De La Rue R M 1999 *Prog. Quantum Electron.* **23** 51

[5] Busch K, Lölkes S, Wehrspohn and Föll H, eds. 2004 *Photonic Crystals* (Berlin: Wiley-VCH)

[6] Baba T, Fukaya N and Yonekura J 1999 *Electron. Lett.* **35** 654

[7] Yamada S, Koyama T, Katayama Y, Ikeda N, Sugimoto Y, Asakawa K, Kawai N and Inoue K 2001 *J. Appl. Phys.* **89** 855

[8] Lončar M, Nedeljković D, Vučković J, Scherer A and Pearsall T P 2000 *Appl. Phys. Lett.* **77** 1937

[9] Tokushima M, Kosaka H, Tomita A and Yamada H 2000 *Appl. Phys. Lett.* **76** 952

[10] Lombardet B, Ferrini R, Dunbar L A, Houdré R, Cuisin, C, Drisse O, Lelarge F, Pommereau F, Poingt F and Duan G-H 2005 *Appl. Phys. Lett.* **86** 111111

[11] Lin S Y, Chow E, Johnson S G and Joannopoulos J D 2000 *Opt. Lett.* **25** 1297

[12] Kawai N, Inoue K, Carlsson N, Ikeda N, Sugimoto Y, Asakawa K and Takemori T 2001 *Phys. Rev. Lett.* **86** 2289

[13] Chow E, Lin S Y, Wendt J R, Johnson S G and Joannopoulos J D 2001 *Opt. Lett.* **26** 286

[14] Talneau A, Le Gouezigou L and Bouadma N 2001 *Opt. Lett.* **26** 1259

[15] Talneau A, Le Gouezigou L, Bouadma N, Kafesaki M, Soukoulis C M and Agio M 2002 *Appl. Phys. Lett.* **80** 547

[16] Märki I, Salt M, Stanley R, Staufer U and Herzig H-P 2004 *J. Appl. Phys.* **96** 6966

[17] Notomi M, Yamada, K, Shinya A, Takahashi J, Takahashi C and Yokohama I 2001 *Phys. Rev. Lett.* **87** 253902

[18] Asano T, Kiyota K, Kumamoto D, Song B-S and Noda S 2004 *Appl. Phys. Lett.* **84** 4690

[19] Lončar M, Nedeljković D, Vučković J, Scherer A, Kuchinsky S and Allan D C 2002 *Appl. Phys. Lett.* **80** 1689

[20] Barclay P E, Srinivasan K, Borselli M and Painter O 2004 *Appl. Phys. Lett.* **85** 4

[21] Tsai D P, Jackson H E, Thiel U, Reddick R C, Sharp S H and Warmack R J 1990 *Appl. Phys. Lett.* **56** 1515

[22] Choo A G, Jackson H E, Thiel U, De Brabander G N and Boyd J T 1994 *Appl. Phys. Lett.* **65** 947; Balistreri M L M, Korterik J P, Kuipers L and van Hulst N F 2001 *Appl. Phys. Lett.* **79** 910

[23] Campillo A L, Hsu J W P, White C A and Jones C D W 2002 *Appl. Phys. Lett.* **80** 2239

[23a] Balistreri M L M, Korterik J P, Kuipers L and van Hulst N F 2000 *Phys. Rev. Lett*. **85**, 294

[24] Balistreri M L M, Gersen H, Korterik J P, Kuipers L and van Hulst N F 2001 *Science* **294** 1080; Gersen H, Klunder D J W, Korterik J P, Driessen A, van Hulst N F and Kuipers L 2004 *Opt. Lett.* **29** 1291

[25] Greffet J-J and Carminati R 1997 *Prog. Surf. Sci.* **56** 133

[26] Bozhevolnyi S I, Vohnsen B and Bozhevolnaya E A 1999 *Opt. Commun.* **172** 171

[27] Bozhevolnyi S I and Vohnsen B 2002 *Opt. Commun.* **212** 217

[28] McDaniel E B, Hsu J W P, Goldner L S and Tonucci R J 1997 *Phys. Rev.* B **55** 10878

[29] Phillips P L, Knight J C, Mangan B J, Russel P St J, Charlton M D B and Parker G J 1999 *J. Appl. Phys.* **85** 6337

[30] Campillo A L, Hsu J W P, White C A and Rosenberg A 2001 *J. Appl. Phys.* **89** 2801

[31] Gérard D, Berguiga L, de Fornel F, Salomon L, Seassal C, Letartre X, Rojo-Romeo P and Viktorovitch P 2002 *Opt. Lett.* **27** 173

[32] Okamoto K, Lončar M, Yoshie T, Scherer A, Qiu Y and Gogna P 2003 *Appl. Phys. Lett.* **82** 1676

[33] Kramper P, Kafesaki M, Soukoulis C M, Birner A, Müller F, Gösele U, Wehrspohn R B, Mlynek J and Sandoghdar V 2004 *Opt. Lett.* **29** 174

[34] Kramper P, Agio M, Soukoulis C M, Birner A, Müller F, Wehrspohn R B, Gösele U and Sandoghdar V 2004 *Phys. Rev. Lett.* **92** 113903

[35] Bozhevolnyi S I, Volkov V S, Arentoft J, Boltasseva A, Søndergaard T and Kristensen M 2002 *Opt. Commun.* **212** 51

[36] Bozhevolnyi S I, Volkov V S, Søndergaard T, Boltasseva A, Borel P I and Kristensen M 2002 *Phys. Rev.* B **66** 235204

[37] Bozhevolnyi S I and Volkov V S 2004 *Phil. Trans. R. Soc. Lond.* A **362** 757

[38] Cluzel B, Gérard D, Pecard E, Charvolin T, Calvo V, Hadji E and de Fornel F 2004 *Appl. Phys. Lett.* **85** 2682

[39] Gersen H, Karle T J, Engelen R J P, Bogaerts W, Korterik J P, van Hulst N F, Krauss T F and Kuipers L 2005 *Phys. Rev. Lett.* **94** 073903

[40] Gersen H, Karle T J, Engelen R J P, Bogaerts W, Korterik J P, van Hulst N F, Krauss T F and Kuipers L 2005 *Phys. Rev. Lett.* **94** 123901

[40a] Flück E, Hammer M, Otter A M, Korterik J P, Kuipers L and van Hulst N F, 2003 *J. Lightwave Technol* **21**, 1384; Flück E, Hammer M, Vos W L, van Hulst N F and Kuipers L 2004 *Photonics and Nanostructures* **2**,

[40b] Engelen R J P, Karle T J, Gersen H, Korterik J P, Krauss T F, Kuipers L and van Hulst N F 2005 *Opt. Express* **13**, 4457

[41] Bozhevolnyi S I 2001 *J. Microsc.* **202** 313

[42] Bozhevolnyi S I and Bozhevolnaya E A 1999 *Opt. Lett.* **24** 747

[43] Phillips P L, Knight J C, Pottage J M, Kakarantzas G and Russell P St J 2000 *Appl. Phys. Lett.* **76** 541

[44] Nesci A, Dändliker R and Herzig H P 2001 *Opt. Lett.* **26** 208

[45] Volkov V S, Bozhevolnyi S I, Borel P I, Frandsen L H and Kristensen M 2005 *Phys. Rev.* B **72** 035118

[46] DME-DualScope^{TM}, Herlev, Denmark

[47] Arentoft J, Søndergaard T, Kristensen M, Boltasseva A, Thorhauge M and Frandsen L 2002 *Electron. Lett.* **38** 274

[48] Vohnsen B and Bozhevolnyi S I 1999 *J. Microsc*. **194** 311

[49] Nesci A, Dändliker R, Salt M and Herzig H P 2002 *Opt. Commun.* **205** 229

[50] Søndergaard T, Arentoft J and Kristensen M 2002 *J. Lightwave Technol.* **20** 1619

[51] Volkov V S, Bozhevolnyi S I and Taillaert D 2004 *Laser Phys. Lett*. **1** 311

[52] Volkov V S, Bozhevolnyi S I, Borel P I, Frandsen L H and Kristensen M 2005 *phys. stat. sol. (c)*, in press

[53] Volkov V S, Bozhevolnyi S I, Borel P I, Frandsen L H and Kristensen M 2005 *Laser Phys. Lett*., submitted

[54] Borel P I, Frandsen L H, Thorhauge M, Harpøth A, Zhuang Y X and Kristensen M 2003 *Opt. Express* **11** 1757

[55] Flück E, Otter A M, Korterik J P, Balistreri M L M, Kuipers L and van Hulst N F 2001, *J. Microscopy* **202** 104

[56] Peeters C, Flück E, Balistreri M L M, Otter A M, Kuipers L and van Hulst N F 2000 *Appl. Phys. Lett*. **77** 142

[57] Bogaerts W, *et al*. 2004 Opt. Express **12** 1583

[58] Veerman J A, Otter A M, Kuipers L and van Hulst N F1998 *Appl. Phys. Lett*. **72** 3115

[59] Flück E 2003 Ph. D. Thesis, University of Twente, ISBN: 90-365-1929-2

[60] Balistreri M L M, Korterik J P, Kuipers L and van Hulst N F 2001 *J. Lightwave Technol*. **19** 1169

[61] Gersen H, Korterik J P, van Hulst N F and Kuipers L 2003 *Phys. Rev. E* **68** 026604

[62] Gersen H, van Dijk E M H P, Korterik J P, van Hulst N F and L. Kuipers 2004 *Phys. Rev. E* **70** 066609

[63] Olivier S, et al., 2001 *Phys. Rev. B* **63** 113311

[64] Agio M and Soukoulis C M 2001 *Phys. Rev. E* **64** 055603(R)

Figure captions

Figure 1. Schematic representation of the collection SNOM operating in (a) intensity or (b) amplitude (and phase) detection mode. (Adapted from [27].)

Figure 2. (a) Schematic layout of the experimental setup. (b) Optical microscope image showing a top view of the central part of the sample, which contains straight PCWs. (Taken from [45].)

Figure 3. (a) Optical microscope image showing a top view of the tapered fibre positioned against the access ridge waveguide. Grey-scale (b) topographical and (c) near-field optical images (25 × 66 μm^2) obtained with a 40-μm-long PCW of sample N1 at the wavelength $\lambda \cong 1520$ nm for TM-polarization.

Figure 4. Gray-scale (a) topographical and (b-d) near-field optical images (21 × 5.25 μm^2) obtained with sample A for TE polarization at the wavelengths $\lambda \cong$ (b) 1520, (c) 1540, and (d) 1570 nm. The images are orientated in the way that the light propagates from left to right. The depth of the topographical image is ~ 150 nm.

Figure 5. Spatial frequency spectrum of the optical image [Fig. 4(c)] obtained with a straight region of PCW at the wavelength of ≅ 1540 nm. Positions of the main peaks fitted to the experimental data indicated with solid lines. Dotted lines indicate combination frequencies that may appear due to the propagating backward PCW modes and/or nonlinear detection.

Figure 6. Group and phase velocities normalized to the speed of light in vacuum for the (a) TM-polarized and (b) TE- polarized PCW mode of sample N1 as functions of the light wavelength. Solid lines (used to guide the eye) represent quadratic approximations by the least-square method. (Taken from [45].)

Figure 7. Gray-scale (a) topographical and (b-f) near-field optical images (5 × 25 μm^2) obtained with a 40-μm-long PCW (sample N1) at the wavelengths $\lambda \cong$ (b) 1500, (c) 1520, (d) 1550, (e) 1590 and

(f) 1630 nm for TM polarization. The images are orientated in the way that the light propagates upwards. (Taken from [45].)

Figure 8. Gray-scale (a) topographical and (b-f) near-field optical images (5×25 μm^2) obtained with a 40-μm-long PCW (sample N1) at the wavelengths $\lambda \cong$ (b) 1500, (c) 1522, (d) 1524, (e) 1560 and (f) 1600 nm for TE polarization. The images are orientated in the way that the light propagates upwards. (Taken from [45].)

Figure 9. Transmission spectra measured with a 10-μm-long PCW of sample N1 (black line corresponds to TM polarization, light gray line – to TE polarization) and 40-μm-long PCW of sample N2 (gray line) plotted together with the results obtained from the averaged cross sections of SNOM images. (Taken from [45].)

Figure 10. (a) Schematic layout of the experimental setup. (b) Scanning electron micrograph of the PC area of the sample containing PCW-based Y-splitter. (Taken from [52].)

Figure 11. Gray-scale (a) topographical and (b) near-field optical images (60×14 μm^2) taken at the wavelength $\lambda \cong 1550$ nm, for TM-polarization. The images are orientated in the way that the light propagates from left to right. (Taken from [52].)

Figure 12. Gray-scale (a, b) topographical and (c - f) near-field optical images taken at the wavelengths $\lambda \cong$ (c, d)1425 and (e, f) 1460 nm for TM-polarization. The sizes of top- and low-row images are 17×17 μm^2 and 9×9 μm^2, respectively. The images are orientated in the way that the light propagates upwards. (Adapted from [52].)

Figure 13. Phase-sensitive SNOM measurements of the region in the close vicinity of the periodic air rod array. a) Topographical information, which shows clearly the 15 air rods in the waveguide ridge. b) Simultaneously with the topography obtained phase information, the cosine of the phase is displayed. Straight phase fronts with a periodicity of the wavelength of light in the materials are visualized. The incoming light propagates from top to bottom. In the air rod region a perturbation of

the phase fronts is observed (dashed oval). This indicates a local change of the effective refractive index at the location where the air rods are introduced. Image size: 5 μm × 4 μm. (Taken from [40a]).

Figure 14. Two-dimensional Fourier transformations analysis of the phase-sensitive SNOM measurement, which consisted of the cosine of the phase times the amplitude of light (Acosφ). a) shows the original data: *A*cosφ. b) Depicts the spatial frequencies as given by the amplitude of the two-dimensional Fourier transformation of Fig. 14a. For a detailed analysis, we have separated the features found in the Fourier transform. The three most dominant features are presented in Figs. 14d, 14f and 14h. To see the contributing details clearly, different intensity normalizations are used for Figs. 14b, 14d, 14f and 14h. Performing an inverse Fourier transformation on these components reveals in all three cases plane waves, which propagate under different angles. Figs. 14c, 14e and 14g correspond to 14d, 14f and 14h, respectively. Fig. 14c shows plane waves under an angle of 0 degrees, which represent the incoming plane waves propagating through the structure. Fig. 14e reveals plane waves propagating under an angle of 15 degrees and Fig. 14g depicts plane waves propagating under an angle of 21 degrees. The image sizes of Fig. 9a, 9c, 9e and 9g is 9.33 μm × 17.23 μm. Fig. 9b, 9d, 9f, and 9h show an area of 10.7 μm^{-1} × 11.6 μm^{-1}. (Taken from [40a]).

Figure 15. a) Schematic representation of a phase-sensitive, time-resolved SNOM measurements, in this case on a PhCW. The optical signal picked up by the coated fibre probe is interferometrically mixed with light from the same laser that has propagated along a reference branch of the interferometer. The reference branch contains an adjustable optical delay line. b) Scanning electron microscope image of a short version of the W3 waveguide under investigation. (Taken from [40]).

Figure 16. Phase-sensitive SNOM measurement for a fixed optical delay of light in a W3 PhCW. Short pulse were coupled into the structure with a wavelength of 1245 nm ($\omega = 0.369$ for a crystal period of 460 nm). a) Measured topography. b) The measured amplitude times the cosine of the phase of the light in the structure. A large variety of spatial frequencies is visible. c) The optical field amplitude only. It is clear that a break up of the incident pulse has occurred due to differences in group velocity of the various excited Bloch modes. (Adapted from [39]).

Figure 17. Experimentally determined dispersion diagram or, in other words, the measured photonic band structure of light in a W3 PhCW. The grey levels indicate the amplitude of the spatial Fourier transform of the optical data obtained for multiple incident wavelengths. To display the full dynamic range of these amplitudes a logarithmic scale is used. Several Bloch modes are clearly visible in 4 Brillouin zones. (Adapted from [39]).

Figure 18. Time-resolved pulse tracking experiment of pulses propagating in a W3 PhCW. a) Topography. b-g) The measured optical amplitude signal in the W3 PhCW for different reference times. The time difference between each frame is 400 fs. It is clear that Bloch modes with differing group velocities have been excited. Bloch modes with different mode profiles are found to have different group velocities. h) The measured position of the centre-of-mass of the various excited Bloch modes as determined after Fourier filtering as a function of time. Group velocities ranging from $0.121 \times c$ to $0.243 \times c$ are found. Extrapolation of the graphs to the start of the waveguide (dotted line) shows that the Bloch modes are not all excited at the same time even though only one original pulse is incident on the structure. (Adapted from [40]).

Figure 19. Experimentally determined band structure for a larger range of optical frequencies than Figure 17. For a frequency of 0.305 a flat dispersion is visible. (Adapted from [40]).

Figure 20. Pulse tracking experiment at a frequency corresponding to the flat band in Figure 19. a) Topography. b-k) Measured optical amplitude signal as a function of delay time. In the wake of the fast lower order mode a complex and stationary optical pattern is visible in the first 25 μm of the PhCW. It persists for 3.6 ps after the excitation pulse has propagated onward. The field pattern moves by less than 0.9 μm in 3 ps, yielding an upper limit for its velocity of c/1000. All the light in the structure after frame 20f has a wave-vector close to the Brillouin zone boundary. (Adapted from [40]).

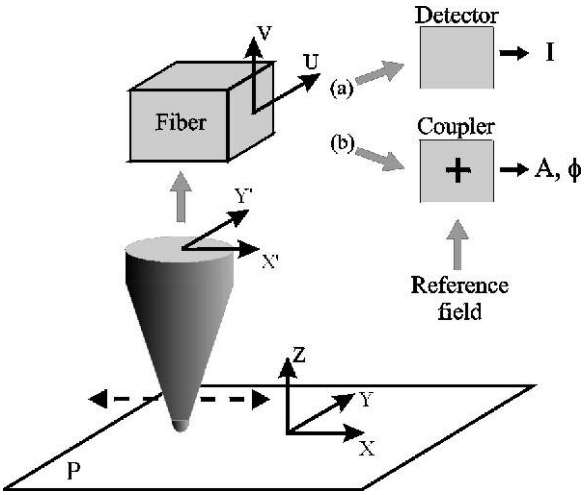
Detector
I
V
U
(a)
Fiber
(b)
Coupler
A, ϕ
Y'
X'
Reference
field
Z
Y
X
P

Fig. 1.

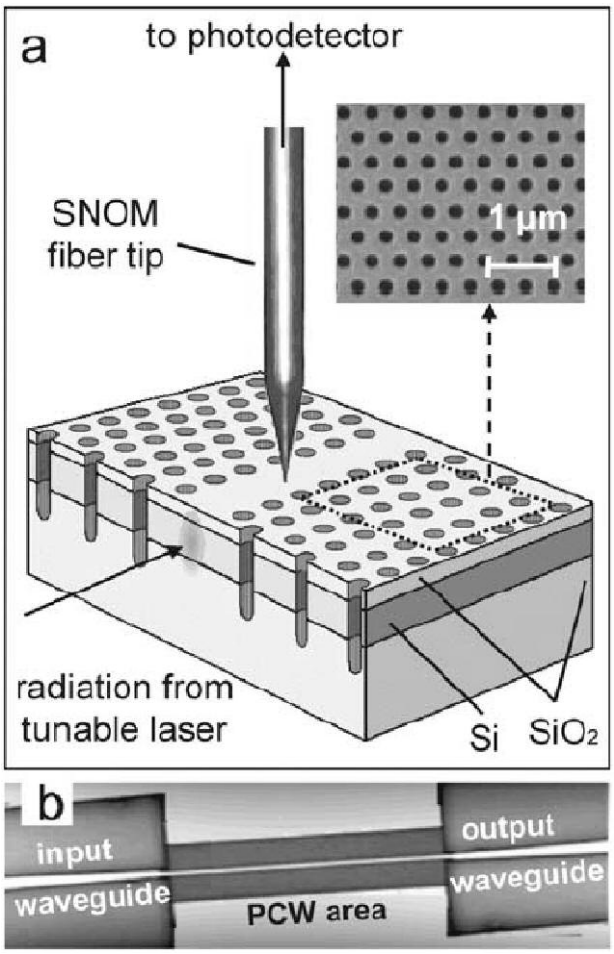
a
to photodetector
SNOM
fiber tip
1 μm
radiation from
tunable laser
Si
SiO2
b
input
waveguide
PCW area
output
waveguide

Fig. 2.

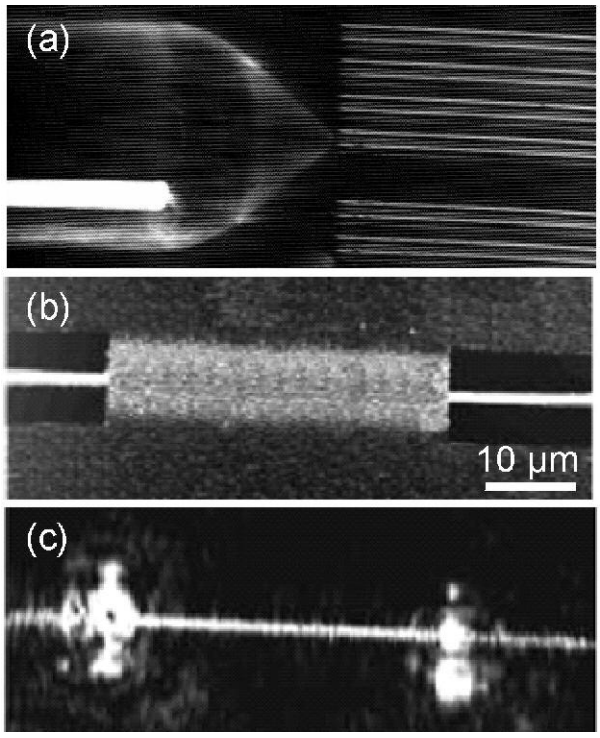

Fig. 3.

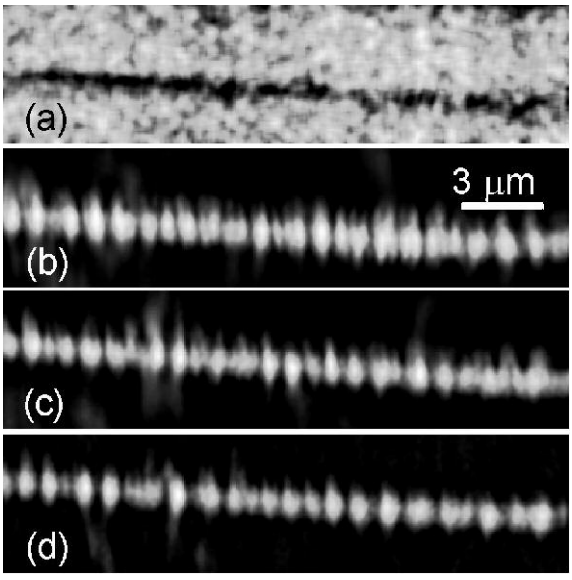

Fig. 4.

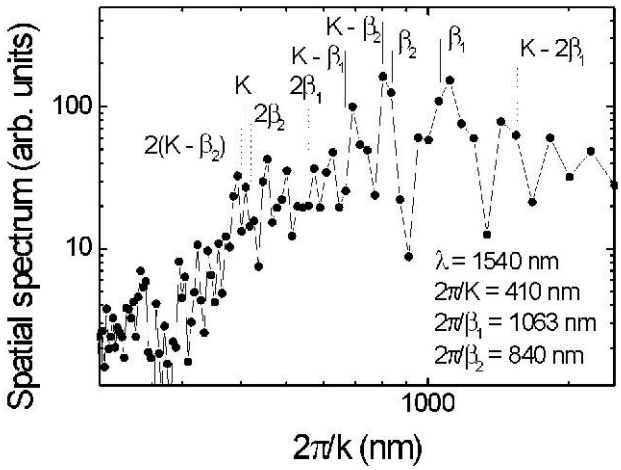
Spatial spectrum (arb. units)
100
10
1000
2π/k (nm)
K
2β2
2(K - β2)
K - β1
2β1
K - β2
β2
β1
K - 2β1
λ = 1540 nm
2π/K = 410 nm
2π/β1 = 1063 nm
2π/β2 = 840 nm

Fig. 5.

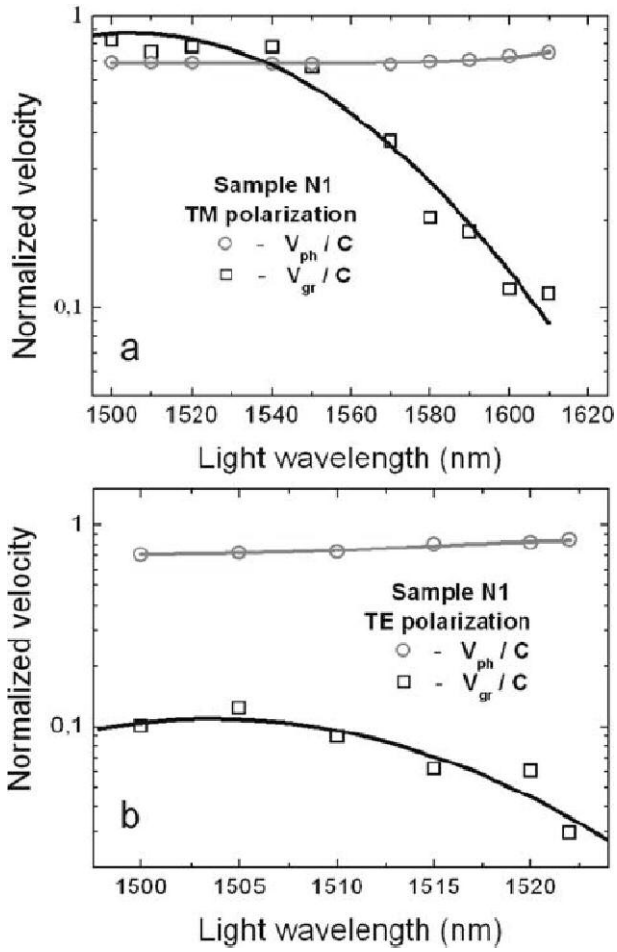
Normalized velocity
1
0,1
Sample N1
TM polarization
- Vph / C
- Vgr / C
a
1500 1520 1540 1560 1580 1600 1620
Light wavelength (nm)
Normalized velocity
1
0,1
Sample N1
TE polarization
- Vph / C
- Vgr / C
b
1500 1505 1510 1515 1520
Light wavelength (nm)

Fig. 6.

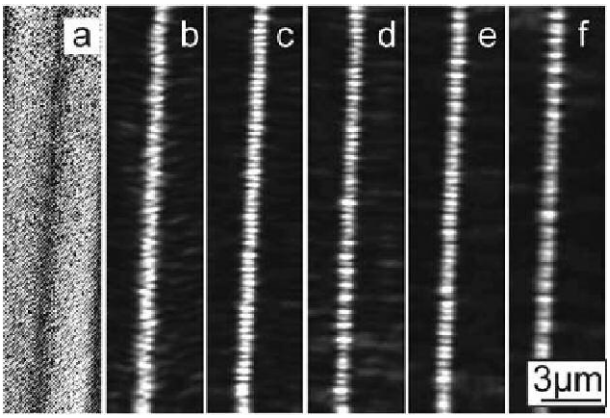

Fig. 7.

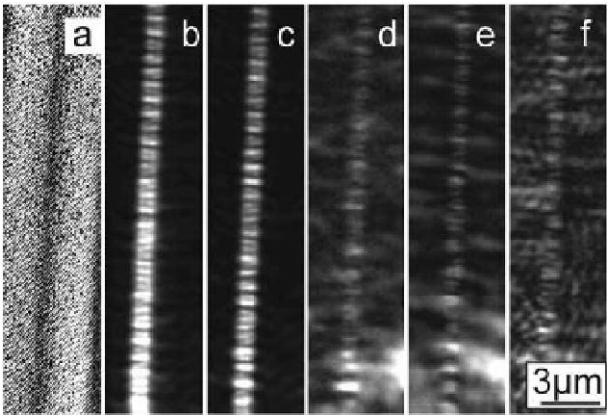

Fig. 8.

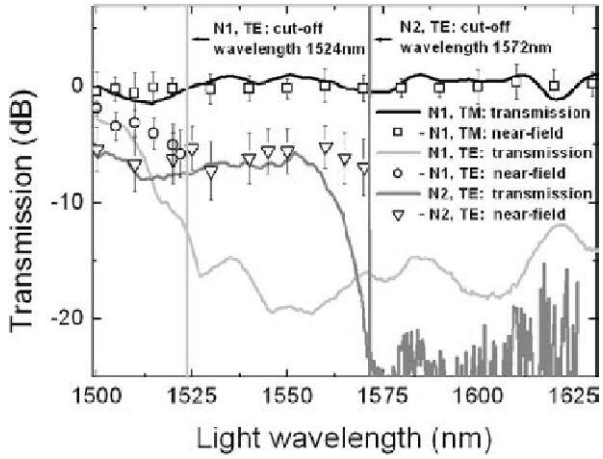

Fig. 9.

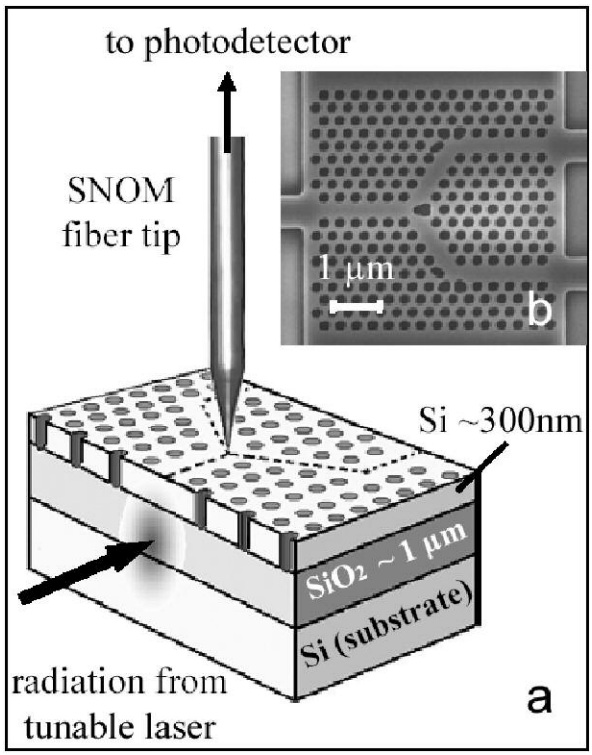

Fig. 10.

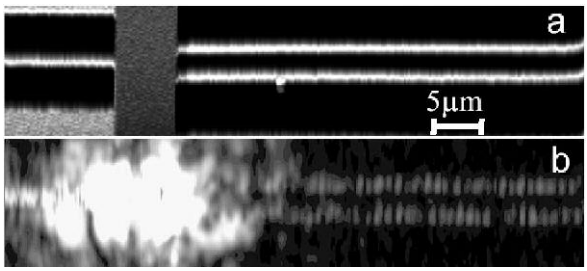

Fig. 11.

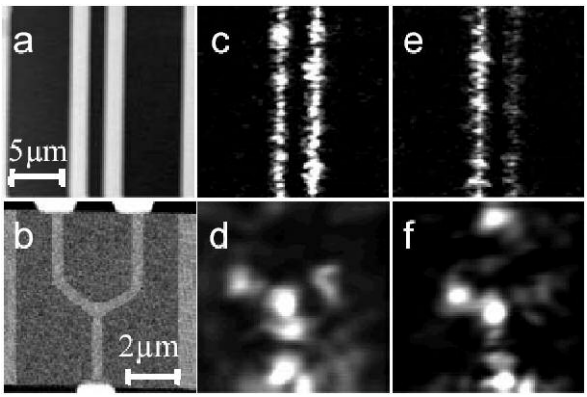

Fig. 12.

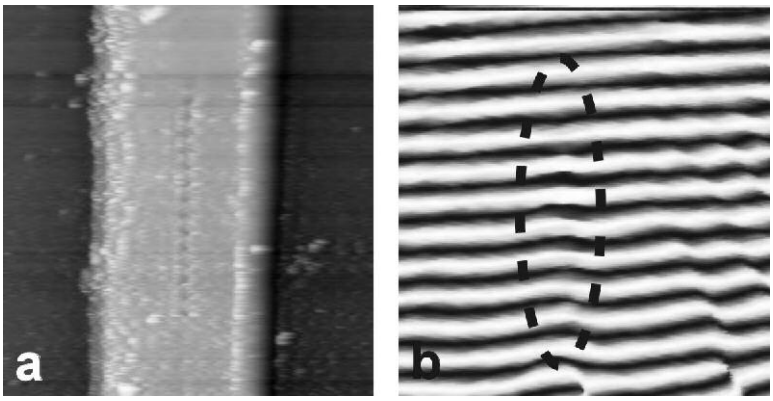

Fig. 13.

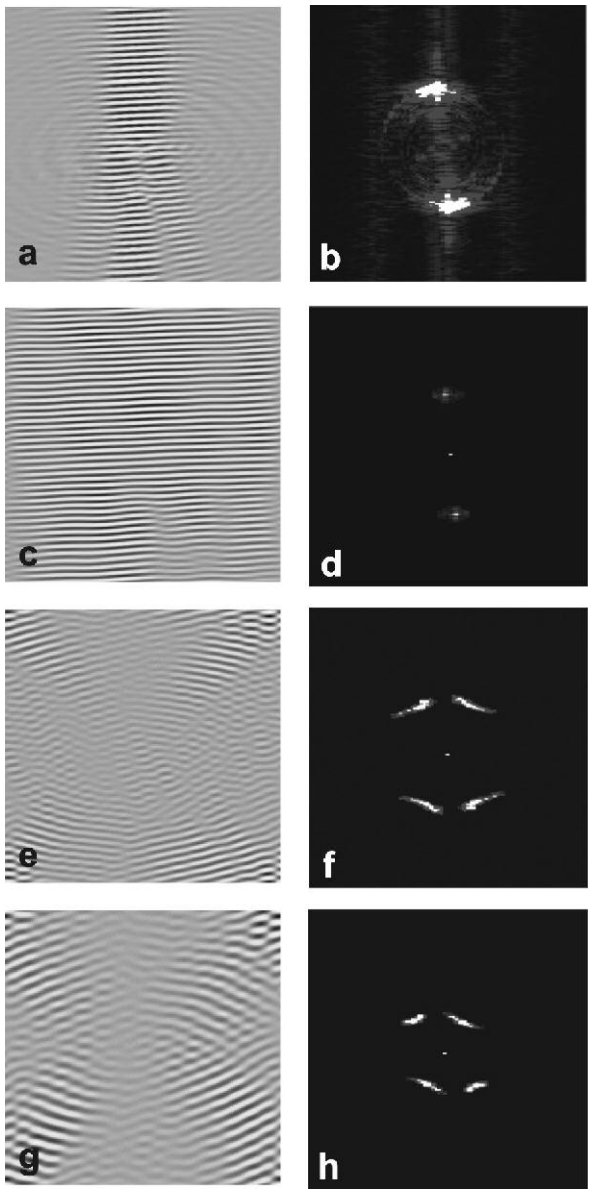

Fig. 14.

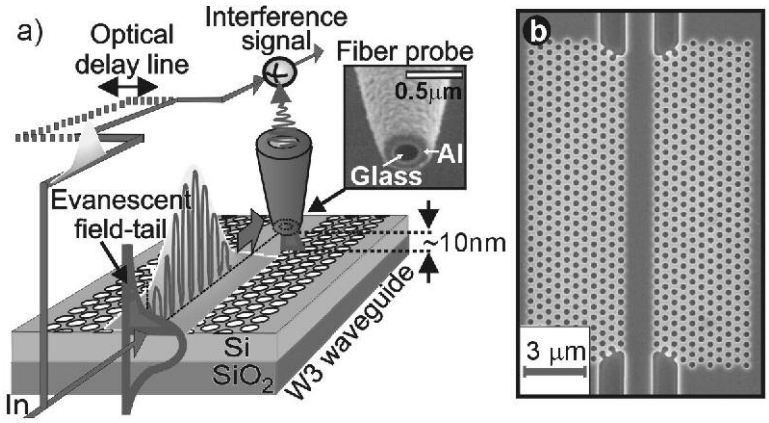

Fig. 15.

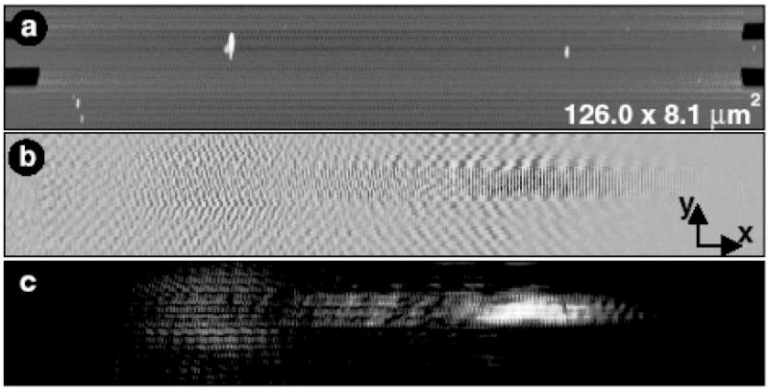

Fig. 16.

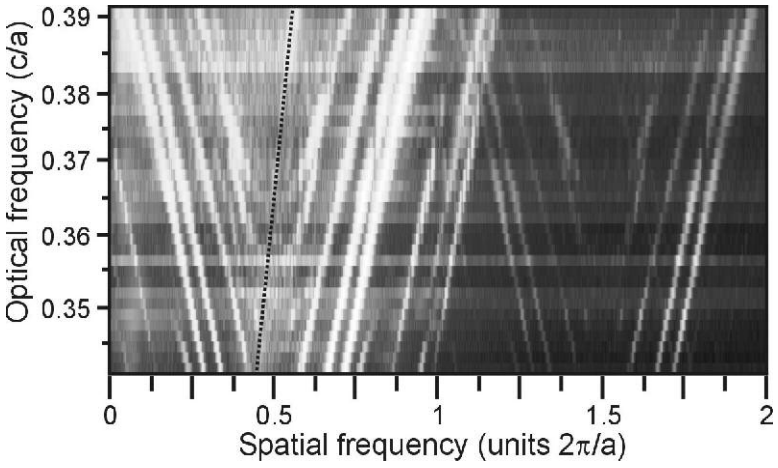

Fig. 17.

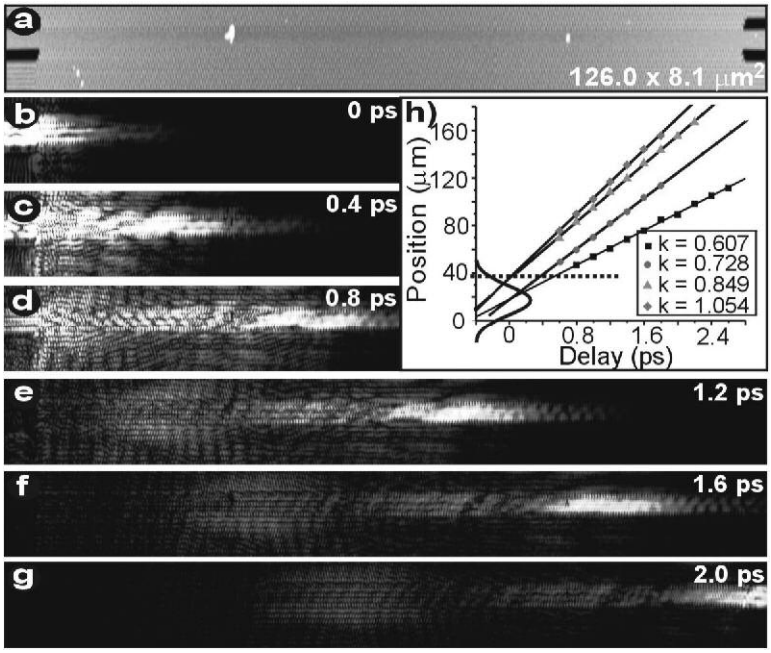
a
126.0 x 8.1 μm²
b
0 ps
c
0.4 ps
d
0.8 ps
h)
Position (μm)
160
120
80
40
0
0
0.8
1.6
2.4
Delay (ps)
k = 0.607
k = 0.728
k = 0.849
k = 1.054
e
1.2 ps
f
1.6 ps
g
2.0 ps

Fig. 18.

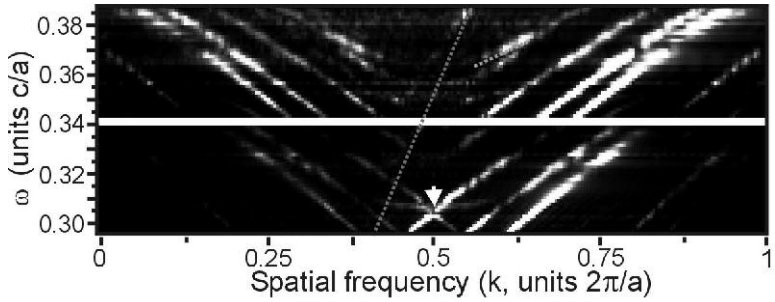
0.38
0.36
0.34
0.32
0.30
ω (units c/a)
0
0.25
0.5
0.75
1
Spatial frequency (k, units 2π/a)

Fig. 19.

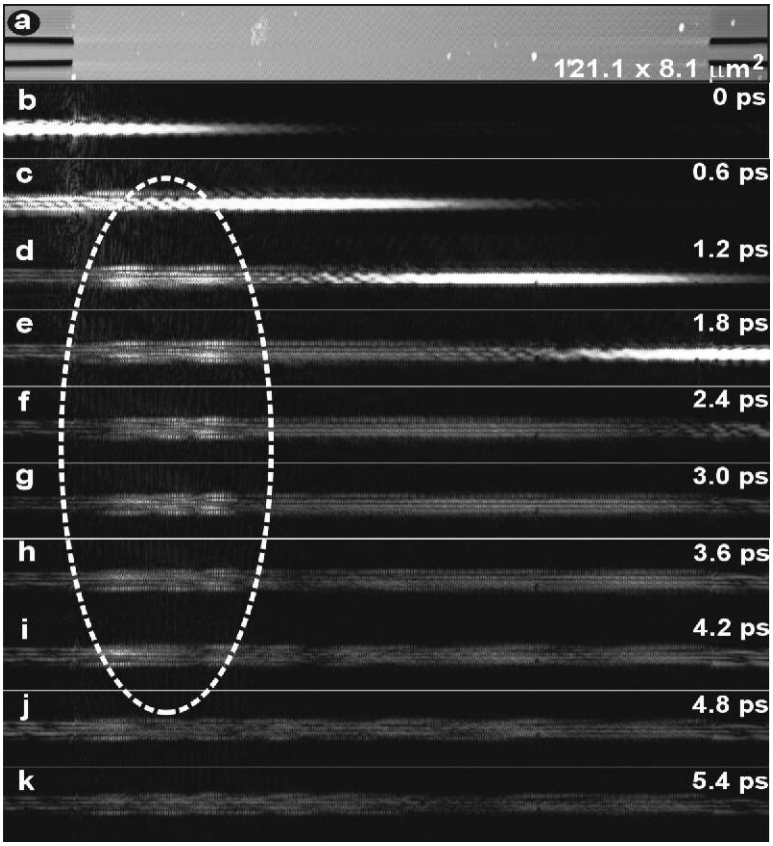
a
121.1 x 8.1 μm²
b
0 ps
c
0.6 ps
d
1.2 ps
e
1.8 ps
f
2.4 ps
g
3.0 ps
h
3.6 ps
i
4.2 ps
j
4.8 ps
k
5.4 ps

Fig. 20.